

## ALOS-2 PALSAR-2 support in GAMMA Software

Urs Wegmüller, Charles Werner, Andreas Wiesmann, Gamma Remote Sensing AG  
 CH-3073 Gümligen, <http://www.gamma-rs.ch>

11-Sep-2014, updated with InSAR example on 30-Nov-2014

### 1. Introduction

JAXA has made available sample data acquired by the ALOS-2 PALSAR-2 instrument [1]. The products made available include SLC data (level 1.1) and geocoded backscatter data (level 1.5) for the following data takes:

Table 1: Sample data from JAXA ([http://www.eorc.jaxa.jp/ALOS-2/en/doc/sam\\_index.htm](http://www.eorc.jaxa.jp/ALOS-2/en/doc/sam_index.htm))

Nr.	Site	Date	Mode	Resolution	Pol.
1	Tokyo, Japan	June 19, 2014	Stripmap	3m	HH+HV
2	Mt. Fuji, Japan	June 20, 2014	Stripmap	3m	HH+HV
3	Amazon, Brazil	June 20, 2014	Stripmap	10m	HH+HV

One of the data sets (Amazon) is acquired in left-looking geometry.

These sample data sets were downloaded by GAMMA and used to conduct an initial adaptation of the GAMMA Software to ALOS-2 PALSAR-2 data processing. Apart from the software adaptation the characteristics of these PALSAR data were assessed – knowing that these data are preliminary and not corresponding entirely to standard PALSAR-2 data.

### 2. PALSAR-2 SLC data import

The sample data included SLC acquisitions in dual-polarization (HH+HV) strip-map mode. To read the data the updated version of the program *par\_EORC\_PALSAR* is used. This program supports reading both PALSAR-1 and PALSAR-2 SLC data in CEOS format. Some of the parameters of the resulting SLC parameter file for the Tokyo data on 20140619 are listed in Table 2.

Table 2 Extract of SLC parameters of the Tokyo data on 20140619 (HH pol. image)

title:	ALOS2003842900-	radar_frequency:	1.2700000e+09 Hz
sensor:	PALSAR2 HH	adc_sampling_rate:	1.0479160e+08 Hz
date:	2014 6 19	chirp_bandwidth:	7.9399998e+07 Hz
start_time:	9788.167000 s	prf:	3120.283000 Hz
azimuth_line_time:	3.2048375e-04 s	azimuth_proc_bandwidth:	2496.22667 Hz
line_header_size:	0	doppler_polynomial:	-38.21725 -1.88377e-05 ...
range_samples:	25312	receiver_gain:	86.0000 dB
azimuth_lines:	31203	calibration_gain:	0.0000 dB
image_format:	FCOMPLEX	sar_to_earth_center:	7005808.7563 m
image_geometry:	SLANT_RANGE	earth_radius_below_sensor:	6371124.3509 m
center_latitude:	35.6177327 degrees	earth_semi_major_axis:	6378137.0000 m
center_longitude:	139.6377864 degrees	earth_semi_minor_axis:	6356752.3141 m
heading:	-170.0618427 degrees	number_of_state_vectors:	11
range_pixel_spacing:	1.430422 m	time_of_first_state_vector:	9490.999535 s
azimuth_pixel_spacing:	2.209140 m	state_vector_interval:	60.000000 s
near_range_slc:	782204.0000 m	state_vector_position_1:	-3692977.4437
incidence_angle:	39.6690 degrees		2046567.9497 5586918.7437 m m m
azimuth_deskew:	OFF	state_vector_velocity_1:	-4147.01826 4622.15721
azimuth_angle:	90.0000 degrees		-4423.35808 m/s m/s m/s

An overview in the entire Tokyo scene and a small section are shown in Figure 1. For the small section shown a 2x2 multi-looking in range and azimuth was used. The Equivalent Number of Looks (ENL) we determined for the section was around 3.8.

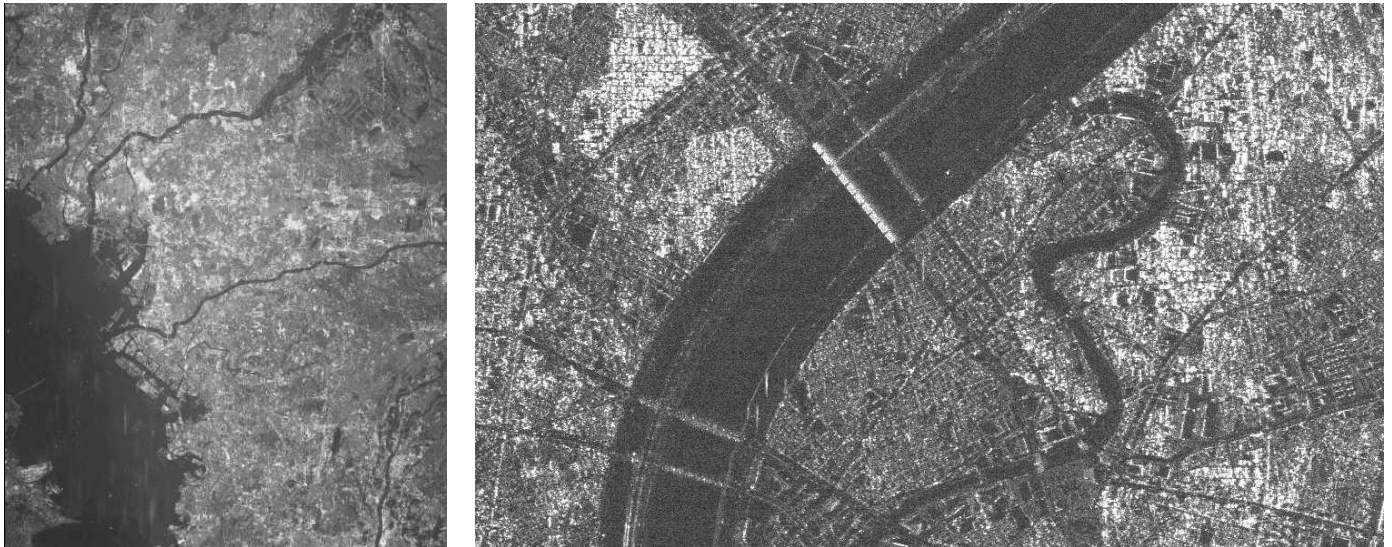


Figure 1 PALSAR-2 data over Tokyo. Full frame (left) showing the wide coverage and small section (right) showing the high spatial resolution of this data set. Both images are in slant-range geometry.

### 3. PALSAR-2 SLC data characteristics

The sample product data were used to assess some characteristics of PALSAR-2.

#### 3.1 Range and azimuth spectra

The program *dismph\_fft* was used to visualize the range and azimuth spectra of the SLC data over Tokyo (Figure 2).

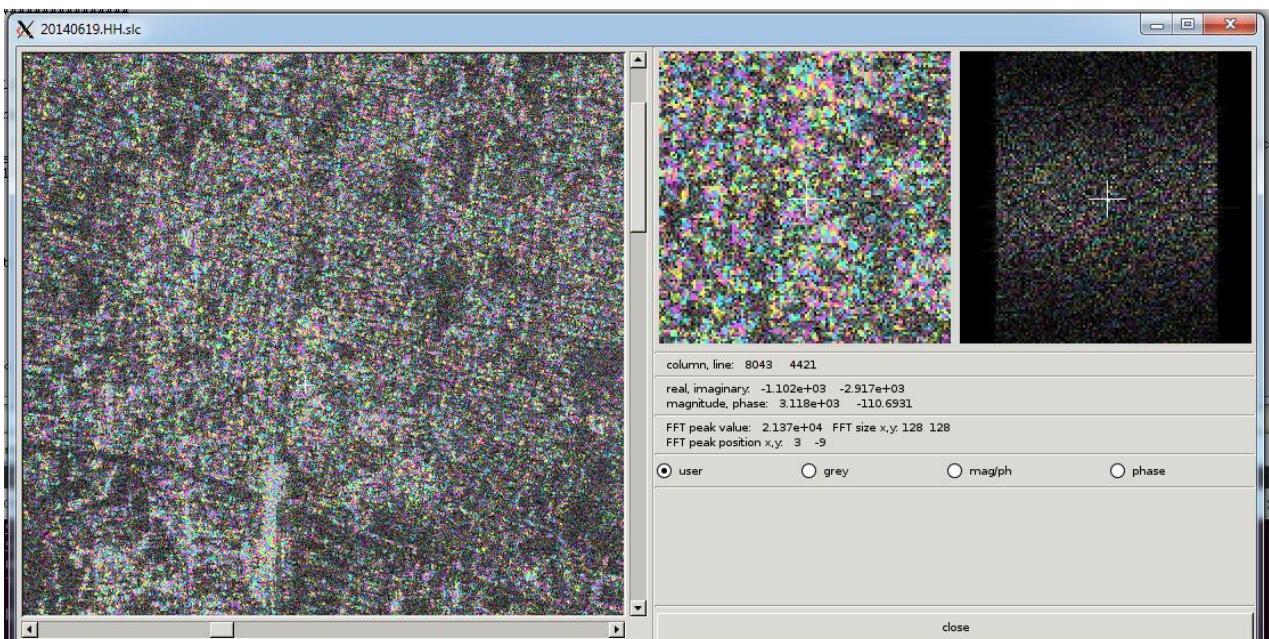


Figure 2 Spectrum of SLC data over Tokyo as visualized by the program *dismph\_fft*.

Then we also determined the azimuth spectrum using the program *az\_spec\_SLC*. The resulting plot is shown in Figure 3.

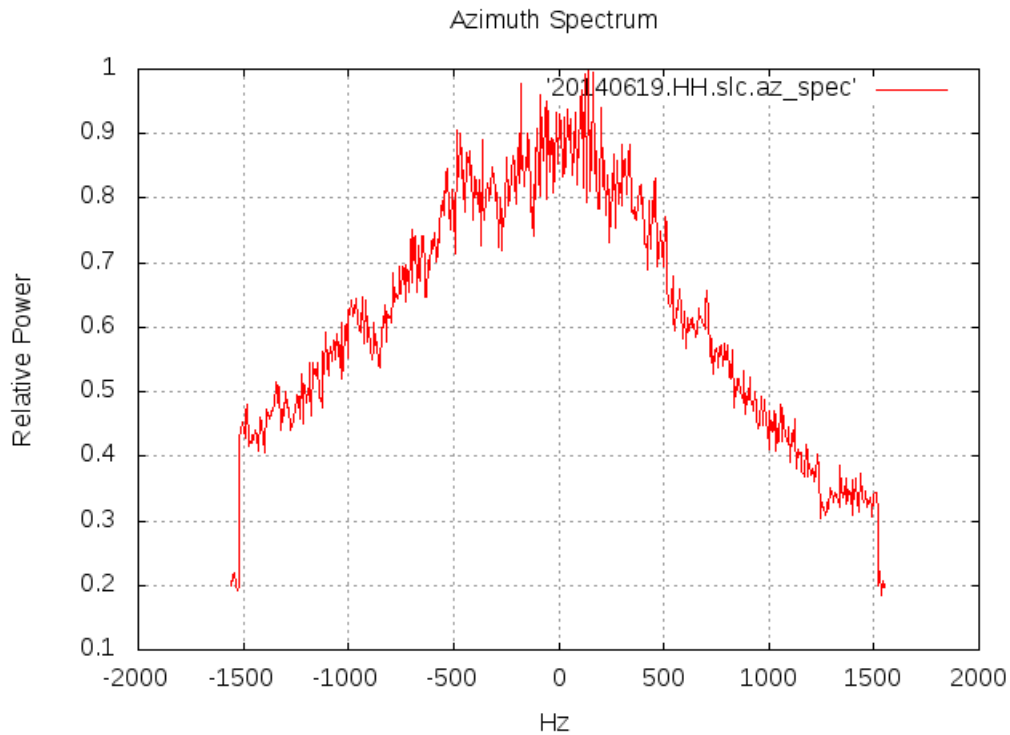


Figure 3. Azimuth spectrum of PALSAR-2 SLC data over Tokyo.

### 3.2 Point target characteristics

Further analysis of the PALSAR-2 SLC was performed to evaluate the point target performance in the image. A bright target was selected and analyzed using the Gamma point target analysis program *ptarg* to evaluate range and azimuth resolution, peak and integrated sidelobe levels and phase characteristic. Plots of range and azimuth cuts of the point target response are shown in Figures 4 and 5. An image of the point, over-sampled by a factor of 16 in range and azimuth is shown in Figure 6. Peak and integrated sidelobe levels are summarized in Table 2.

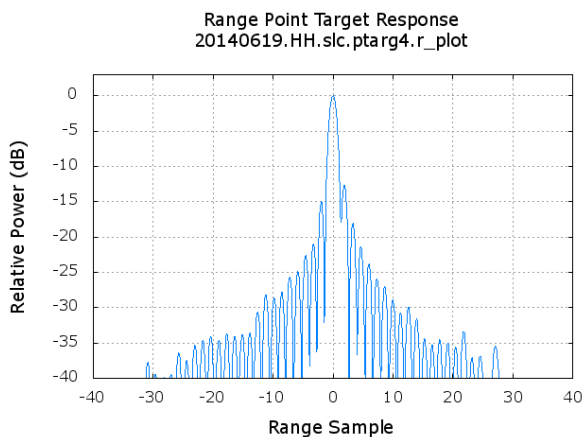


Figure 4 Point target response in range.

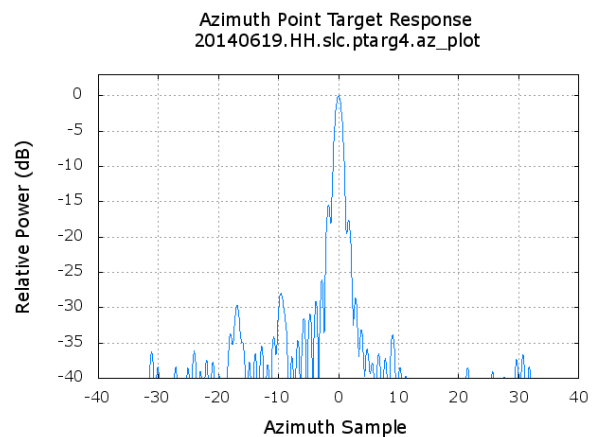


Figure 5 Point target response in azimuth.

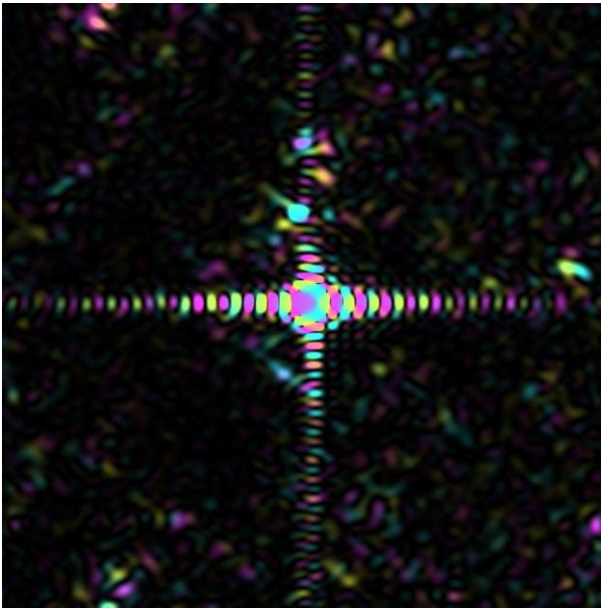


Figure 6. Over-sampled point target response.  
The color scale covers the phase range 0 to  $2\pi$ .

Table 2 Point target resolution, peak side-lobe, and integrated side-lobe levels in range and azimuth

range -3 dB width (samples):	1.185
range -10 dB width (samples):	2.020
range PSLR (dB):	-12.642
range ISLR (dB):	-11.389
azimuth -3 dB width (samples):	1.079
azimuth -10 dB width (samples):	1.880
azimuth PSLR (dB):	-15.545
azimuth ISLR (dB):	-15.860

### 3.3 Quality of SLC focusing

Using the program *af\_SLC* the quality of the focusing of the SAR processing can be assessed. Applying the program to the HH-pol. PALSAR-2 SLC over Tokyo showed that the focusing was not optimal for this processing. We notice a significant non-zero azimuth offset between azimuth spectral sub-look images (approx. -0.42 azimuth pixel) that suggests a velocity correction of around 0.11m/s to achieve an optimal focusing. To further investigate the azimuth offset between azimuth spectral sub-look images we determined offsets between azimuth sub-looks. For the Amazon data no significant azimuth offset between azimuth spectral sub-look images was found (< 0.03 azimuth pixel), confirming an excellent focusing.

Table 3 *af\_SLC* command used and information autofocus quality information retrieved (as written by the program to standard output).

```
af_SLC 20140619.HH.slz.par 20140619.HH.slz 512 2048 1024 4096 10. 1 0 af_SLC.offsets1 2
```

number of valid autofocus patch estimates after culling: 182

nominal image center effective focus velocity (m/s): 7242.9648

average autofocus velocity (m/s): 7242.6979

average range offset between looks (pixels): 0.01849

average azimuth offset between looks (pixels):-0.41928

average velocity delta (m/s): -0.1132

estimated autofocus velocity poly. coeff.: vel.x: 7242.8462 vel.y: -1.354e-04 acc.x: 0.000e+00

autofocus velocity std. dev.(m/s): 0.1050

average velocity std. dev. (m/s): 0.0078

nominal azimuth chirp rate (from state vectors) (Hz/sec\*\*2): -555.3788

estimated azimuth chirp rate error (Hz/sec\*\*2): 0.0174

estimated azimuth quadratic phase error (deg.): 15.780

estimated SLC phase error (deg.): 5.260

SLC focus quality (TBW \* chirp\_rate\_error/chirp\_rate): 0.351

NOTE: focus quality values > 2 indicate peak broadening > 8 percent

### 3.4 Split-beam positional offsets

Azimuth offsets between azimuth spectral sub-band images can relate to imperfect focusing or to along-track variations in the ionospheric path delay [2]. To determine the azimuth offset field for the SLC data over Tokyo we first applied band-pass filtering to the SLC data to determine 2 azimuth sub-band SLC with center frequencies shifted plus and minus a quarter of the prf and with a filtered bandwidth of 0.4 of the prf

```
bpf 20140619.HH.slc 20140619.HH.slc.lf 25312 0.0 1.0 -0.25 0.4 0 0 - - 0 0 1.0 128
bpf 20140619.HH.slc 20140619.HH.slc.hf 25312 0.0 1.0 0.25 0.4 0 0 - - 0 0 1.0 128
```

Then we determined the offsets between the lower and upper azimuth band SLC using

```
create_offset 20140619.HH.slc.par 20140619.HH.slc.par 20140619.off 1 50 50 0
```

followed by

```
offset_pwr_tracking 20140619.HH.slc.lf 20140619.HH.slc.hf 20140619.HH.slc.par
20140619.HH.slc.par 20140619.off 20140619.sb_offs 20140619.sb_snr 256 128 - 2 3. 50 50 -
- - - 4 0
```

We determined then the bi-linear offset polynomial and rejected offset estimate outliers using

```
offset_fit 20140619.sb_offs 20140619.sb_snr 20140619.off 20140619.sb_coffs - 3.0 1 0
```

→

```
final range offset poly. coeff.: -0.00136
final range offset poly. coeff. errors: 1.55117e-05
final azimuth offset poly. coeff.: -0.20470
final azimuth offset poly. coeff. errors: 3.78543e-05
final model fit std. dev. (samples) range: 0.0395 azimuth: 0.0964
```

which indicates a significant non-zero average azimuth offset of around -0.2 azimuth pixels (of the SLC). No significant non-zero range offset was observed.

To display the azimuth offset field we extract the imaginary part of the culled offset field (program *cpx\_to\_real*) and visualize the values using a color scale between offsets of -0.5 pixel (red) and +0.5 pixel (blue, see Figure 7. Based on the data alone it is difficult to judge if the reason for the azimuth offsets observed relate to the processing or to ionospheric effects as there is no obvious azimuth striping in the offsets but mainly an overall trend.

For the Amazon data no significant azimuth offsets between azimuth spectral sub-look images were found.

For the Mt Fuji data an azimuth offset between azimuth spectral sub-look images similar to the one for the Tokyo data was found (-0.25 pixel), with a spatial variation that might relate to ionospheric effects.

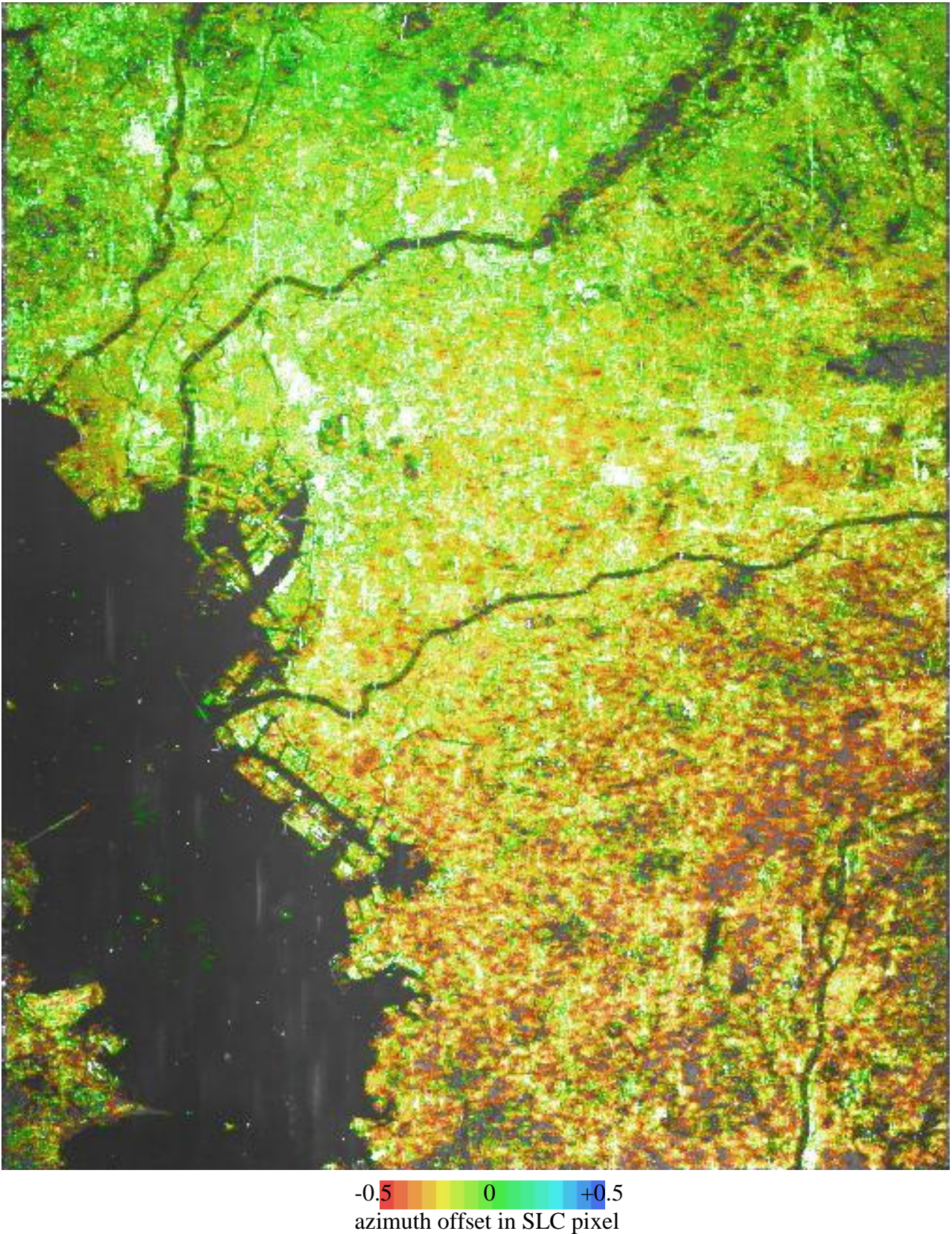


Figure 7. Azimuth offsets between azimuth sub-band SLC images of the PALSAR-2 Tokyo sample data.

#### 4. Geocoding

The multi-look intensity image was terrain corrected geocoded using the SRTM-3" DEM available from USGS as height reference. As positional reference the SRTM, respectively backscatter values simulated based on the SRTM DEM could not be used reliably for the Tokyo data as the area is flat and therefore the simulated backscattering does not show sufficient features that can be used in the refinement. We used therefore as positional reference a geocoded PALSAR scene over a part of the area that we had available. The output terrain geocoded image is shown in Figure 8.



Figure 8 Terrain corrected geocoded HH-pol. PALSAR-2 image of Tokyo acquired on 19-Jun-2014.

For the Amazon data the refinement based on the SRTM DEM worked well with relatively small final model fit standard deviations of 0.256 sample in range and 0.093 sample in azimuth, correcting only a positional offset.

## 5. Dual-polarization

The SLC data over Tokyo is acquired in dual-polarization mode (HH+HV). We imported the HV polarization data and checked if there is a positional offset between the HH and the HV images. No significant non-zero positional offsets were identified. This is also confirmed by the polarization composite shown in Figure 9.

Furthermore we determined the phase and the coherence between HH and HV. In many parts, but clearly not everywhere, the coherence between the two polarizations is very low (Figure 10). To avoid misinterpretation of the phase in those areas with very high phase noise the HH – HV image phase difference is only shown for areas with a coherence  $> 0.3$  (Figure 11).

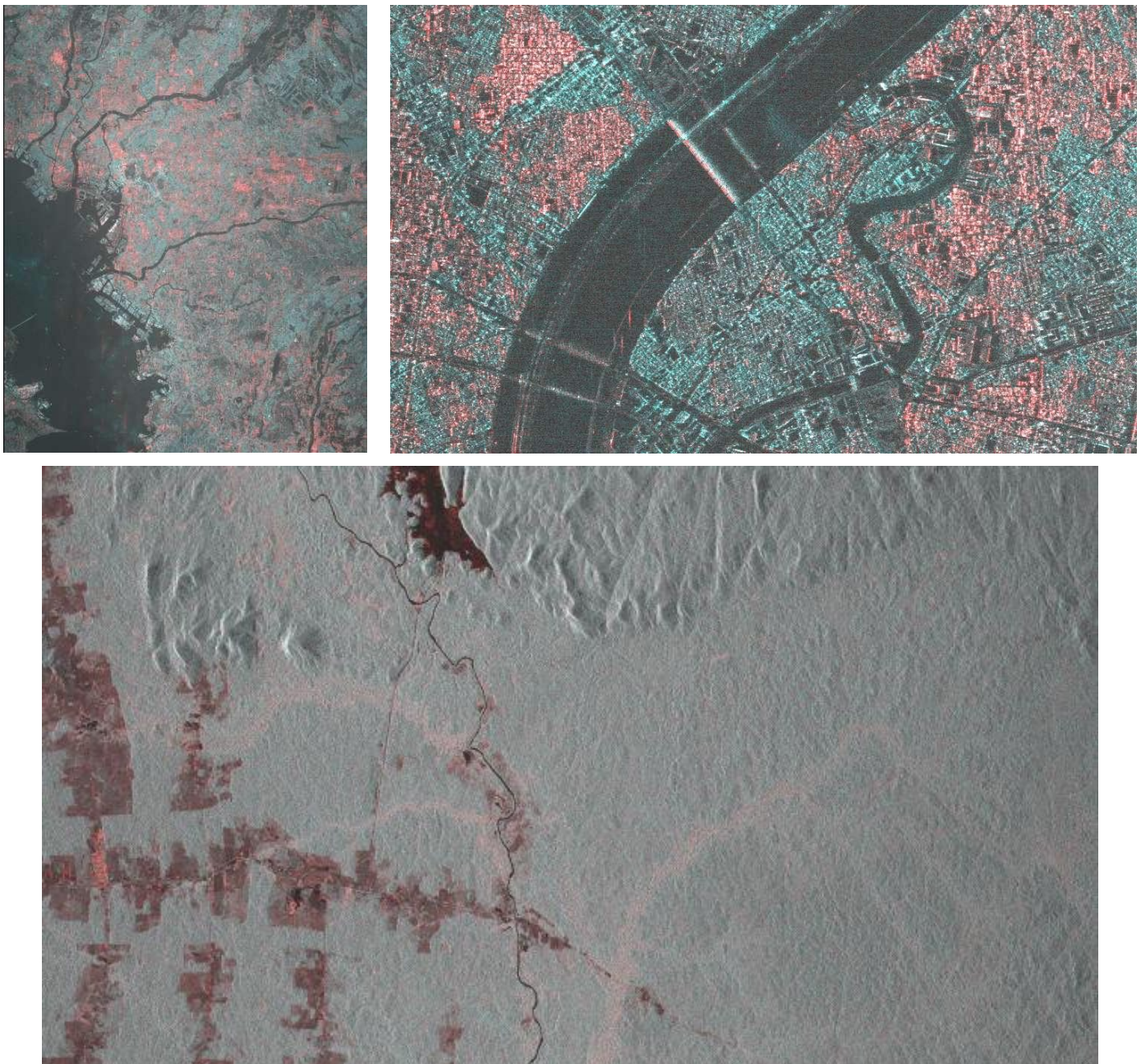


Figure 9 PALSAR-2 RGB composite of HH backscatter in red channel and HV backscatter in green and blue channel. Full frame (top left) and small section (top right) as over Tokyo in Figure 1, and over the Amazon (bottom). The reddish color indicates areas with rather low HV backscatter and cyan areas with rather high HV backscatter relative to the HH backscattering over the same areas.



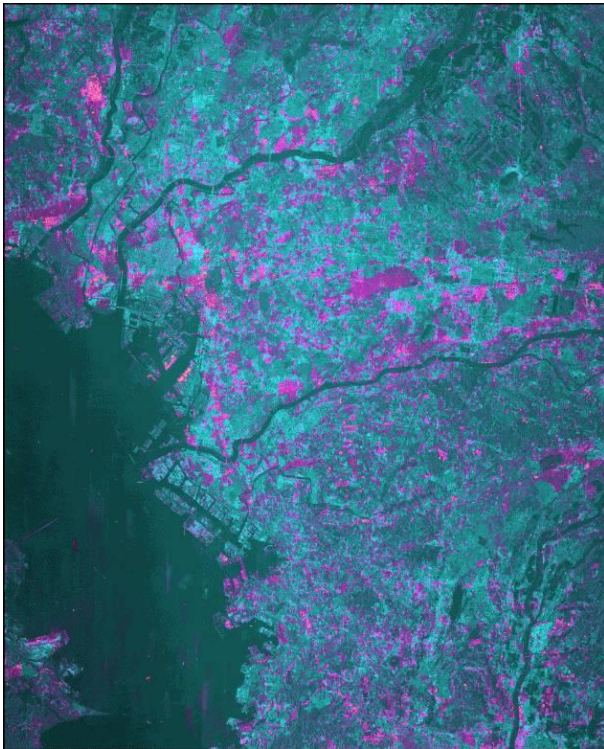


Figure 10 HH to HV coherence

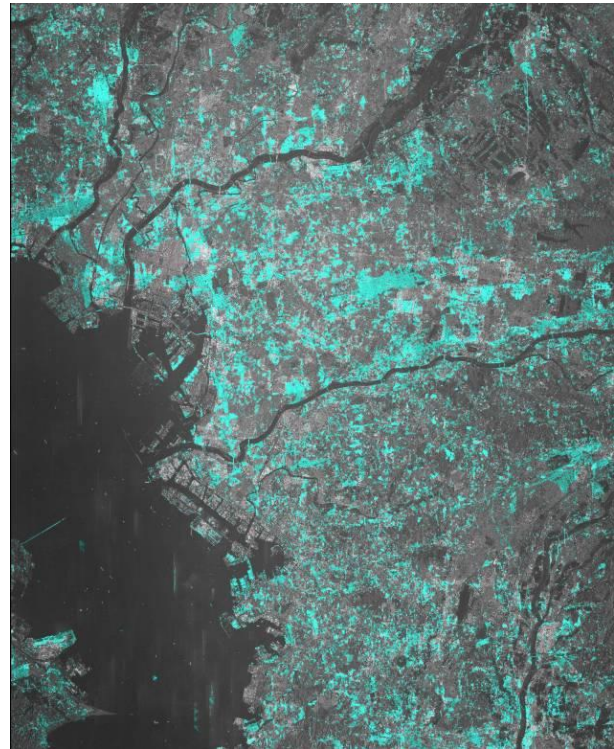


Figure 11 HH to HV phase difference (one phase cycle corresponds to one color cycle).

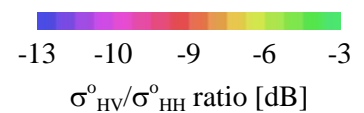
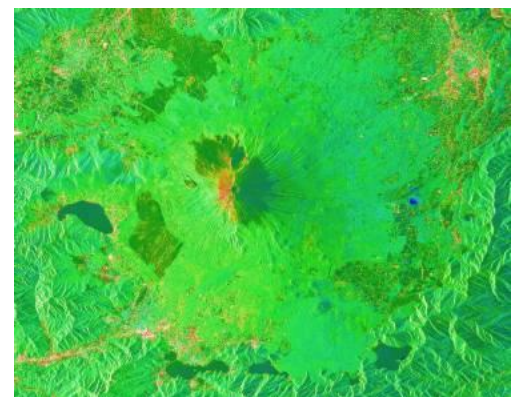
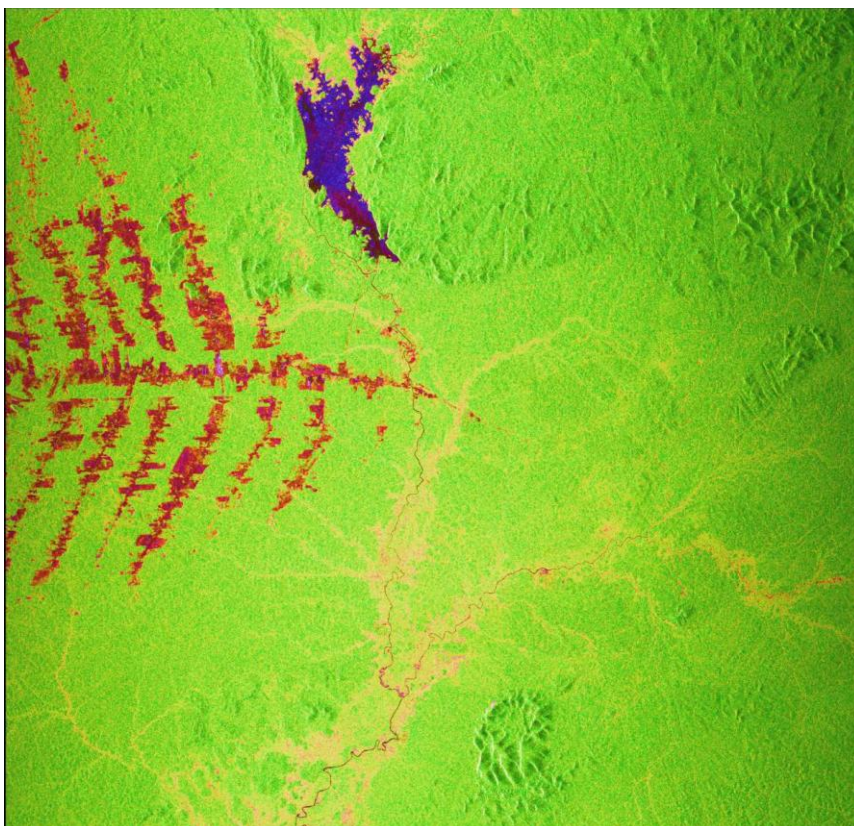


Figure 12 As examples of a polarization parameter calculated from the HH and HV pol. backscattering the  $\sigma_{HV}^o/\sigma_{HH}^o$  ratio in dB using a color scale as indicated for the ratio and the HH-pol. backscattering as the image brightness is shown for the Amazon (left) and Mt Fuji (right).

Another composite based on the HH and HV pol. backscattering shown over the Amazon and over Mt. Fuji is the polarization ratio (Figure 12). The polarization ratio clearly discriminates deforested areas from undisturbed forest. Over areas with very low backscattering we observe clear indications that the noise equivalent sigma zero (NESZ) is affecting the observed HV backscatter. Over smooth water surfaces (as present in the Mt Fuji data) a very low HV/HH ratio would be expected. Nevertheless, the NESZ increases the HV image value resulting in values comparable to forest!

## 6. Backscatter normalization of terrain topography effects

To retrieve normalized backscattering coefficients terrain topography effects on the pixel area need to be corrected for. In the GAMMA Software this can be done using the program *pixel\_area*. The effect is well demonstrated using the backscattering over the Amazon forest (Figure 13). The backscattering of the northern part is clearly influenced by the terrain topography. This influence disappears almost completely when compensating the effect pixel area as estimated based on the SRTM DEM heights.

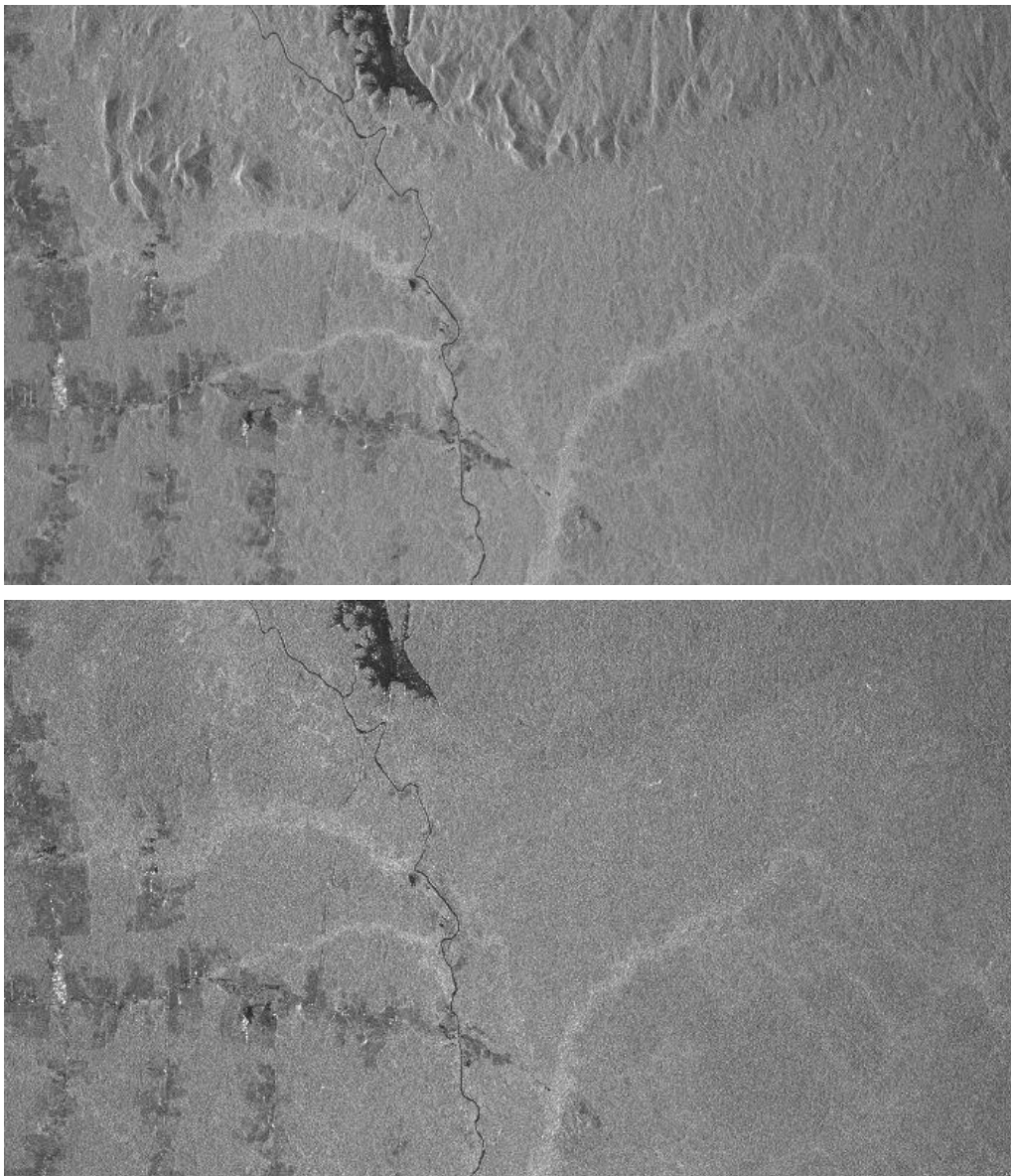


Figure 13 PALSAR-2 HH backscatter over the Amazon without (top) and with (bottom) normalization of terrain topography effects (pixel area) on the backscattering normalization.  $\gamma^0$  values are shown to also reduce the influence of the incidence on the backscattering.

## 7. Level 1.5 data

The program `par_EORC_PALSAR_geo` reads the PALSAR-2 level 1.5 data and generates an SLC parameter file as well as a DEM parameter file. The SLC parameter file contains acquisition related parameters that define e.g. the related slant range geometry. The DEM parameter file contains the information on the ground sampling of the image data and on the projection indicated in the meta data. The image file geometry is neither slant range (as defined in the SLC parameter file) nor the map projection indicated in the DEM parameter file and so the data cannot be georeferenced using the GAMMA software tools. As an example the level 1.5 data over Mt. Fuji are shown in Figure 14.

The geometry is a ground-range – azimuth geometry but we are not sure about the exact slant range to ground-range transformation that was performed. The values are amplitudes (not intensities).

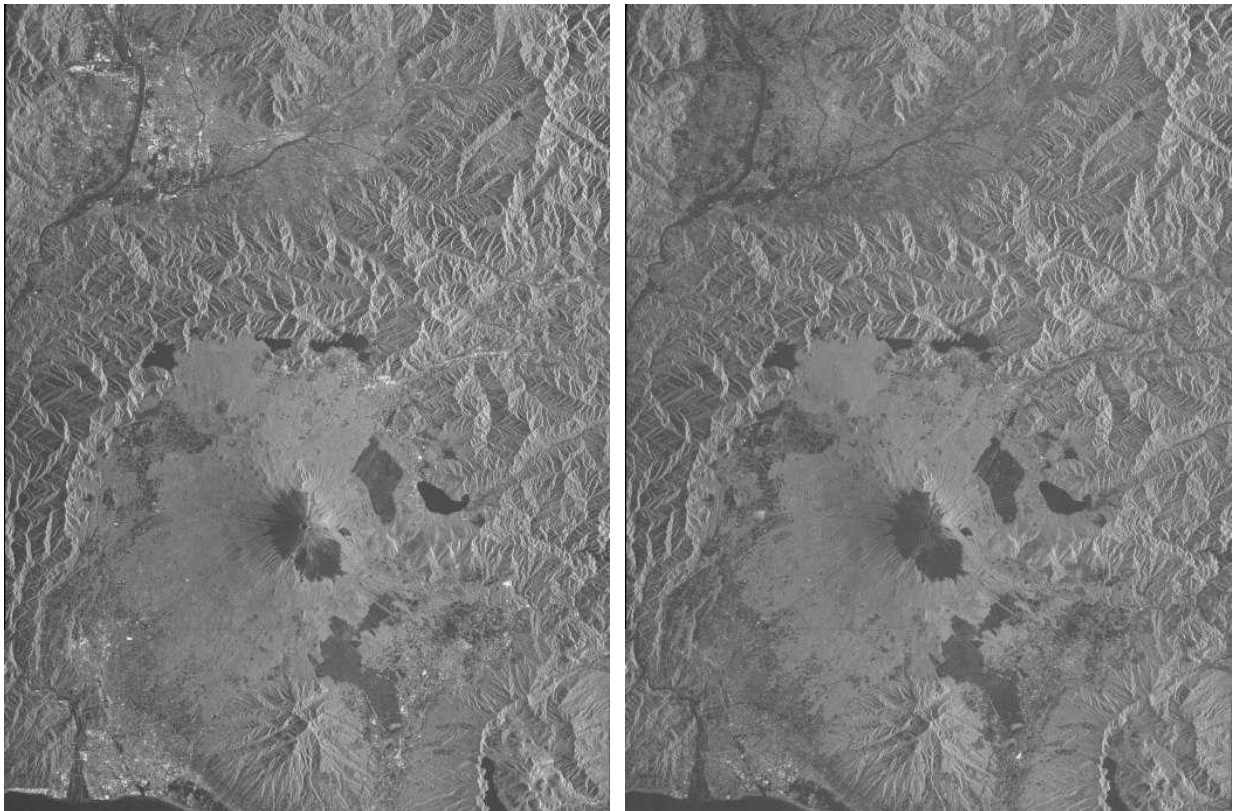


Figure 14 PALSAR-2 HH (left) and VV (right) backscatter Mt Fuji (level 1.5 CEOS sample product).

## 8. Interferometry using PALSAR-2 strip-map mode data

For PALSAR-2 strip-map mode data SAR interferometry is supported in the same way as for PALSAR-1. Figure 15 shows a differential interferogram generated using two HH-pol acquisitions acquired in dual-polarization mode over the Swiss alps on 20140906 and 20141115 with a spatial baseline of about 147 m (perpendicular component). Over the higher elevations the coherence is very low because of changing snow conditions.

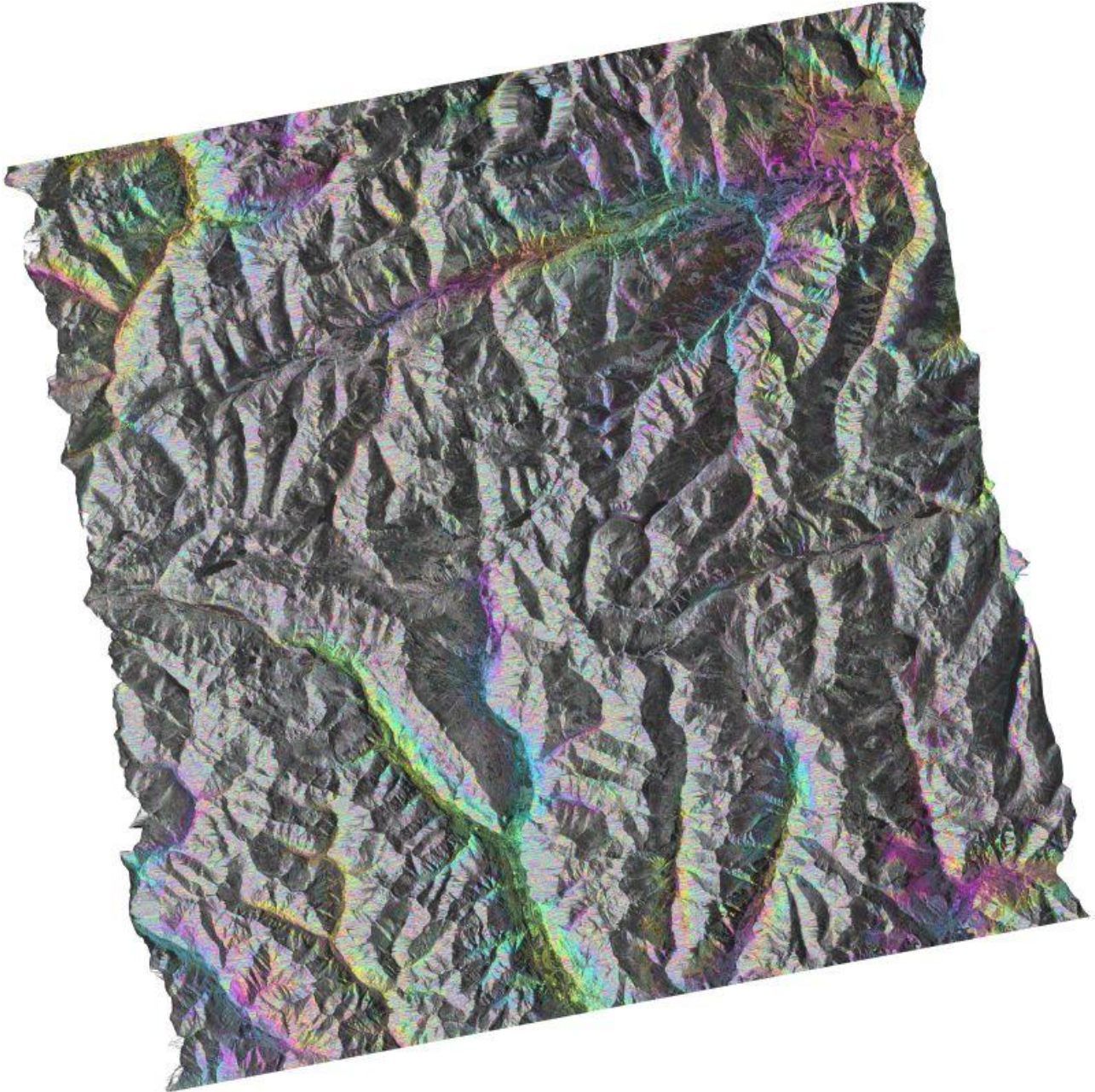


Figure 15: PALSAR-2 differential interferogram using HH-pol acquisitions acquired in dual-polarization mode over the Swiss alps on 20140906 and 20141115 ( $B_{\text{perp}}$  147m, dt 98 days). One color cycle corresponds to one phase cycle. The full frame is shown, geocoded to Swiss national coordinates.

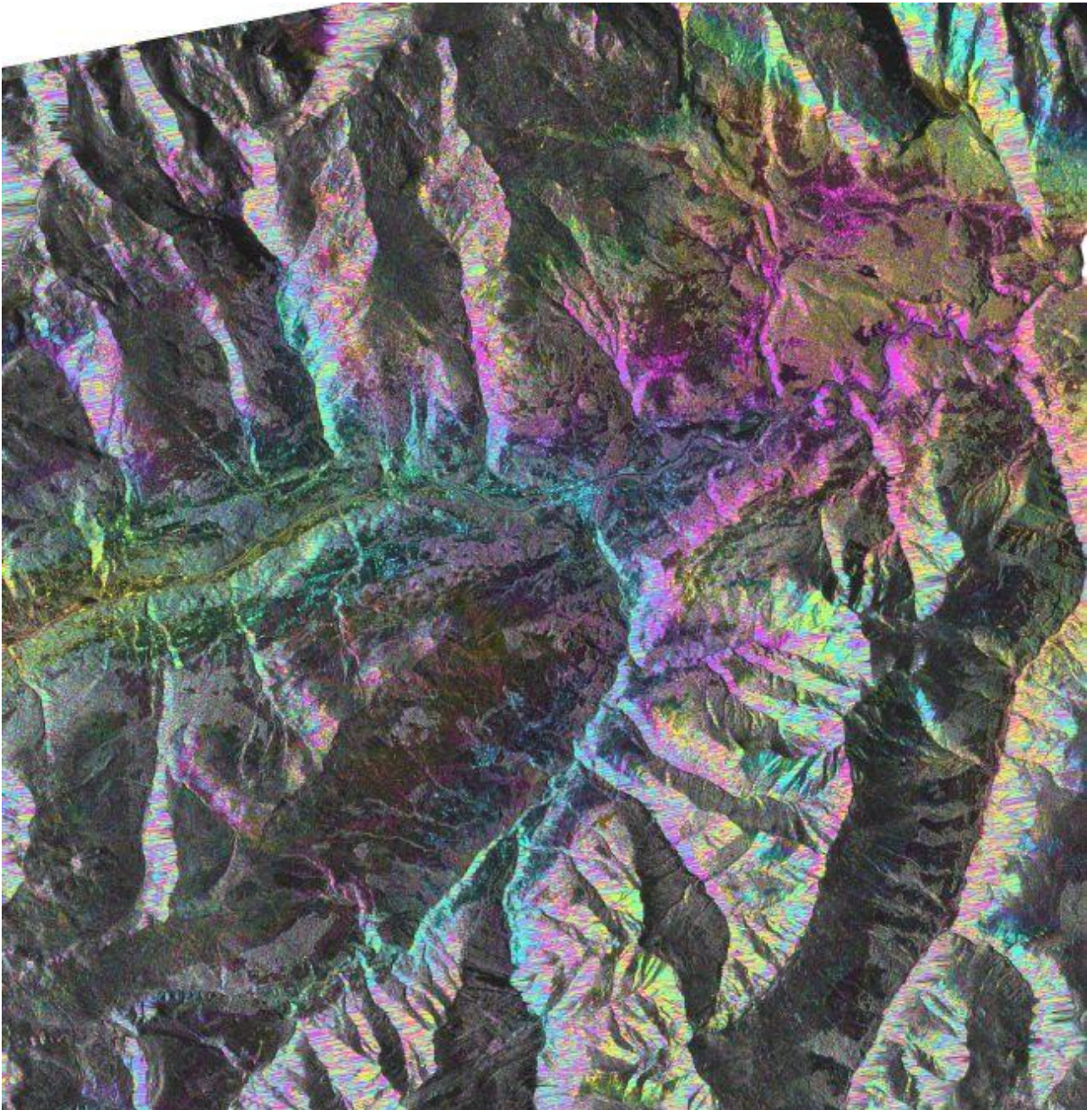


Figure 16: 26km x 26 km section of PALSAR-2 differential interferogram in Figure 15 over Flims-Illanz-Lumnez (Grison, Switzerland). One color cycle corresponds to one phase cycle.

## 9. References

[1] [http://www.eorc.jaxa.jp/ALOS-2/en/doc/sam\\_index.htm](http://www.eorc.jaxa.jp/ALOS-2/en/doc/sam_index.htm)

[2] Wegmüller U., C. Werner, T. Strozzi, and A. Wiesmann, “Ionospheric electron concentration effects on SAR and INSAR”, Proc. IGARSS 2006, Denver, Colorado, USA, 31- Jul. – 4. Aug. 2006.

## 10. Acknowledgment

The original data are provided by JAXA as the ALOS-2 sample products [1]; © JAXA.